Available online at www.sciencedirect.com
SCIENCE @ DIRECT®
Thin Solid Films 455–456 (2004) 14–23
thin solid films
www.elsevier.com/locate/tsf

Multichannel Mueller matrix ellipsometer based on the dual rotating compensator principle

Chi Chen, Ilsin An, G.M. Ferreira, N.J. Podraza, J.A. Zapien, R.W. Collins*

Department of Physics and Materials Research Institute, The Pennsylvania State University, University Park, PA 16802, USA

Abstract

A multichannel ellipsometer in the dual rotating-compensator configuration has been designed and constructed for applications in real time Mueller matrix ellipsometry (approx. 2–5 eV) of anisotropic surfaces and films. The sequence of optical elements for this instrument is denoted $PC_{1r}(\omega_1)SC_{2r}(\omega_2)A$, where P, S, and A represent the polarizer, sample, and analyzer. $C_{1r}(\omega_1)$ and $C_{2r}(\omega_2)$ represent two MgF_2 biplate compensators that rotate at frequencies of $\omega_1/2\pi=10$ Hz and $\omega_2/2\pi=6$ Hz, synchronized for a ratio ω_1:ω_2 of 5:3. Spectra in the 16 Mueller matrix elements of a transmitting or reflecting sample can be established from the 25 non-zero Fourier coefficients of the irradiance waveform *acquired in a single 0.25* s *optical cycle*. Initial high speed Mueller matrix measurements have been performed on weakly anisotropic samples that push the instrument to its precision/accuracy limits. These include the (110) Si surface with maximum cross-polarization ellipsometric angles of $\psi_{ps}\sim0.1°$ and nanostructured thin films with maximum $\psi_{ps}\sim1°$.

Keywords: Multichannel Mueller matrix ellipsometry; Dual-rotating compensator ellipsometer; Data reduction; Ellipsometer calibration; Optical anisotropy

1. Introduction

Multichannel ellipsometers have been developed and applied as powerful tools for studying thin film growth and surface modification [1]. The simplest such instruments, used since ~1990, are based on rotating-polarizer principles [2] and have several limitations. The most serious one arises from the inability of a rotating polarizer to measure the third normalized Stokes vector component of the light beam reflected from the sample [3]. Thus, precision/accuracy is degraded for analysis of reflected polarized light having a small ellipticity angle χ. In addition, unrecognized depolarization generates experimental errors. Since ~1997, rotating-compensator multichannel ellipsometers have been used that overcome these limitations by providing all three components of the Stokes vector [4]. These instruments provide high precision/accuracy spectra in χ over its full range ($-45°\leq\chi\leq45°$), and, thus as the sign of χ (inaccessible by rotating polarizer). In addition, the rotating-compensator instrument provides the degree of polarization of the reflected beam, which reveals sample non-uniformities and/or instrument errors.

For optically anisotropic materials, even the single rotating-compensator multichannel ellipsometer may be insufficient for real time characterization. The ultimate solution in this case is to measure the entire Mueller matrix of the sample, while retaining the high speed required for real time spectroscopy. A number of Mueller matrix ellipsometer designs have been proposed, including configurations with dual rotating-compensators [5–8] or phase modulators [9]. Other designs require multiple measurements in different optical configurations, and so are unsuitable for real time materials analysis [10–14]. In this study, the performance and applications are reported for a recently-developed multichannel Mueller matrix ellipsometer designed in the $PC_{1r}(\omega_1)SC_{2r}(\omega_2)A$ configuration as described in Ref. [8] (see Fig. 1). The polarization generation arm includes a fixed polarizer and rotating compensator, and the polarization detection arm includes a second rotating compensator and fixed analyzer. With a frequency ratio ω_1:ω_2 of 5:3, this instrument provides the entire Mueller matrix at ~150 spectral positions from ~2 to 5 eV in

*Corresponding author. Tel.: +1-814-865-3059; fax: +1-814-865-2326.
E-mail address: rwc6@psu.edu (R.W. Collins).

0040-6090/04/$ - see front matter © 2003 Elsevier B.V. All rights reserved.
doi:10.1016/j.tsf.2003.11.191

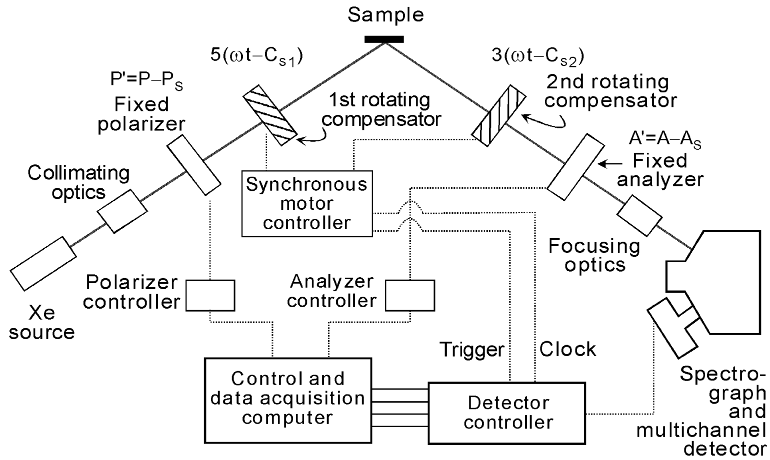

Fig. 1. Schematic diagram of the dual rotating-compensator multichannel ellipsometer.

a time as short as 0.25 s, a single optical period of the dual rotating-compensators.

2. Theoretical description

For the dual rotating-compensator multichannel ellipsometer with $\omega_1 = 5\omega$ and $\omega_2 = 3\omega$, the time-dependent waveform predicted at each pixel of the array detector can be expressed in terms of the Mueller matrix of the sample [8]. The waveform used for theoretical analysis is given by

$$I(t) = i_0 \left\{ a_0 + \sum_{n=1}^{16} \left[a_{2n}\cos(2n\omega t - \phi_{2n}) + b_{2n}\sin(2n\omega t - \phi_{2n}) \right] \right\}, \tag{1a}$$

where $\{a_0, (a_{2n}, b_{2n}); n = 1,\ldots,16\}$ define the d.c. and unnormalized a.c. Fourier coefficients. Among the 32 possible a.c. Fourier coefficients under the summation in Eq. (1a), the eight coefficients with $n = 9$, 12, 14 and 15 vanish even for the most general Mueller matrix. The phases of the individual Fourier components, $\{\phi_{2n}; n = 1,\ldots,8, 10, 11, 13, 16\}$ in Eq. (1a) are given in terms of the phase angles (C_{S1}, C_{S2}) of the two rotating compensators as follows:

$$\phi_{2n} = \{\mathrm{sgn}(3L - 5K)\}\{3LC_{S2} - 5KC_{S1}\};$$

$$(K = 0, 2, 4;\ L = 0, 2, 4), \tag{1b}$$

where $2n = |3L - 5K|$, applicable for $n = 1,\ldots, 7, 10$; and

$$\phi_{2n} = 3LC_{S2} + 5KC_{S1}; \quad (K = 2, 4;\ L = 2, 4), \tag{1c}$$

where $2n = 3L + 5K$, applicable for $n = 8$, 11, 13, 16. Here, (C_{S1}, C_{S2}) are defined by the equations $C_1' = 5(\omega t - C_{S1})$ and $C_2' = 3(\omega t - C_{S2})$, where C_1' and C_2' are the true angles of the fast axes of the first and second compensators. Thus, $-5C_{S1}$ and $-3C_{S2}$ are the angles of the fast axes at $t = 0$, defined as the onset of data acquisition for the given pixel (or pixel group). The d.c. and d.c.-normalized a.c. coefficients can be written collectively as $\{I_0, (\alpha_{2n}, \beta_{2n}); n = 1,\ldots,16\}$ and are given by $I_0 = a_0 i_0$, $\alpha_{2n} = a_{2n}/a_0$, and $\beta_{2n} = b_{2n}/a_0$. The average irradiance in the waveform I_0 can be expressed as the product of three factors (i) the ellipsometer spectral response function I_{00}, (ii) the d.c. coefficient a_0, and (iii) the (1,1) Mueller matrix element M_{11} of the sample.

3. Data collection

For an error-free system in the dual-rotating compensator configuration with the angular frequencies $\omega_1 = 5\omega = 2\pi(10)\ \mathrm{s}^{-1}$ and $\omega_2 = 3\omega = 2\pi(6)\ \mathrm{s}^{-1}$, the irradiance at any given pixel (or pixel group) obeys the following experimental expression [8]:

$$I'(t) = I_0' \left\{ 1 + \sum_{n=1}^{16} (\alpha_{2n}' \cos 2n\omega t + \beta_{2n}' \sin 2n\omega t) \right\}, \tag{2}$$

where $\{I_0', (\alpha_{2n}', \beta_{2n}'); n = 1, 2,\ldots, 16\}$ are the d.c. and d.c.-normalized a.c. Fourier coefficients to be determined experimentally. Eq. (2) differs from Eq. (1a) in that the former waveform does not include the compensator phase angles ϕ_{2n}. These terms are omitted from the experimental phases because they cannot be determined until a calibration is performed that yields (C_{S1}, C_{S2}). If the detector is read N times per fundamental optical period $(\pi/\omega) = 0.25$ s, each read-out with the same exposure time of $t_e = \pi/(N\omega) = (4N)^{-1}$ s, then N irradiance waveform integrals are generated. For $N = 36$ and $t_e = 6.94$ ms, one can form a set of 36 equations in

36 unknowns for each spectral position by extending the series in Eq. (2) to include all even Fourier coefficients up to β_{36}' (but not including α_{36}'). The corresponding 36×36 matrix of coefficients can be inverted to deduce $\{I_0', \alpha_{2m}' \ (m=1,\ldots,17), \beta_{2n}' \ (n=1,\ldots,18)\}$. Of these 36 quantities, 11 Fourier coefficients should vanish (corresponding to m, $n=9$, 12, 14, 15, 17; $n=18$).

4. Data reduction

Once the d.c. and normalized a.c. Fourier coefficients $\{I_0', (\alpha_{2n}', \beta_{2n}'); n=1,\ldots,8, 10, 11, 13, 16\}$ are determined and calibration data for (C_{S1}, C_{S2}) are available (see Section 5), the next step is a phase correction of the coefficients performed by applying

$$(\alpha_{2n}\ \beta_{2n})^T=\Re(\phi_{2n})(\alpha_{2n}'\beta_{2n}')^T;$$
$$(n=1, 2,\ldots, 8, 10, 11, 13, 16) \tag{3}$$

where T denotes the transpose of the row vector and $\Re(\phi_{2n})$ is the 2×2 rotation transformation matrix for the angle ϕ_{2n} [8]. From the phase-corrected Fourier coefficients, the normalized Mueller matrix elements $\{m_{ij}=M_{ij}/M_{11}; i=1,\ldots,4; j=1,\ldots,4\}$ can be determined. For the upper left 3×3 block of m_{ij}, there is only one possible set of equations for this purpose, whereas for the 4th row and column, multiple methods are possible. Here, the following set of equations is applied:

$$a_0=t_1t_2\{t_1t_2+\alpha_8\cos4(P'-A')+\beta_8\sin4(P'-A') -t_1\alpha_{12}\cos4A'-t_1\beta_{12}\sin4A' -t_2\alpha_{20}\cos4P'-t_2\beta_{20}\sin4P' +\alpha_{32}\cos4(P'+A')+\beta_{32}\sin4(P'+A')\}^{-1}, \tag{4a}$$

$$m_{12}+im_{13}=(a_0/s_1t_2)\exp(-2iP')\times\{-B_8\exp(4iA')+t_2B_{20}-B_{32}\times\exp(-4iA')\}, \tag{4b}$$

$$m_{14}=(a_0/t_2\sin\delta_1)\{2\alpha_{22}\sin2(P'+2A') -2\beta_{22}\cos2(P'+2A')-t_2\alpha_{10}\sin2P' +t_2\beta_{10}\cos2P'\}, \tag{4c}$$

$$m_{21}+im_{31}=(a_0/t_1s_2)\exp(-2iA')\times\{-B_8^*\exp(4iP')+t_1B_{12}-B_{32}\times\exp(-4iP')\}, \tag{4d}$$

$$m_{22}+im_{23}=(a_0/s_1s_2)\exp(-2iP')\{B_8\exp(2iA') +B_{32}\exp(-2iA')\}, \tag{4e}$$

$$m_{24}+im_{34}=(-2ia_0/s_2\sin\delta_1)\{B_{22}\exp[-2i(P'+A')]\}, \tag{4f}$$

$$m_{32}+im_{33}=(ia_0/s_1s_2)\exp(-2iP')\{B_8\exp(2iA') -B_{32}\exp(-2iA')\}, \tag{4g}$$

$$m_{41}=(a_0/t_1\sin\delta_2)\{2\alpha_{14}\sin2(2P'-A') -2\beta_{14}\cos2(2P'-A')+t_1\alpha_6\sin2A' -t_1\beta_6\cos2A'\}, \tag{4h}$$

$$m_{42}+im_{43}=(2ia_0/s_1\sin\delta_2)\{B_{26}\exp[-2i(P'+A')]\}, \tag{4i}$$

$$m_{44}=(2a_0/\sin\delta_1\sin\delta_2)\{-\alpha_4\cos2(P'-A') -\beta_4\sin2(P'-A')\}, \tag{4j}$$

along with $M_{11}=I_0/(I_{00}a_0)$. In Eqs. (4a)–(4j), $B_{2n}=\alpha_{2n}+i\beta_{2n}$, $B_{2n}^*=\alpha_{2n}-i\beta_{2n}$, $s_j=\sin^2(\delta_j/2)$, and $t_j=\tan^2(\delta_j/2)$ $(j=1,2)$, where δ_j $(j=1,2)$ represent the slow-to-fast axis phase shifts for the first and second rotating compensators. For the evaluation of $M_{ij}=M_{11}m_{ij}$ from $\{I_0, (\alpha_{2n}, \beta_{2n}), n=1,\ldots,8, 10, 11, 13, 16\}$ in data reduction, one requires I_{00}, δ_1, δ_2, $P'=P-P_S$, $A'=A-A_S$, all of which are determined in calibration. Here P' and A' are the true angles of polarizer and analyzer transmission axes given in terms of nominal readings, P and A, and offset corrections, P_S and A_S.

5. Calibration

For the dual rotating-compensator multichannel ellipsometer, the usual calibration sequence involves: (i) measurement of the retardance spectra δ_1 and δ_2 in straight-through, (ii) determination of the optical element offset and phase angles (P_S, C_{S1}, C_{S2}, A_S) with the sample in place after its alignment, and (iii) measurement of the ellipsometer spectral response I_{00} from initial measurements of the starting sample [15]. Thus, with this sequence, δ_1 and δ_2 are determined once in the initial development of the ellipsometer (or after any major system realignment) using the straight-through $PC_{1r}(5\omega)C_{2r}(3\omega)A$ configuration without a sample. The offset and phase angles are determined in a separate step after mounting and aligning the sample. Although self-calibration (i.e. calibration using the measured Fourier coefficients without a separate step) is possible for an isotropic sample, higher accuracy is achieved by performing calibration vs. polarizer and analyzer angular readings. Finally, slight differences in beam path through the second compensator, resulting when measuring samples with differing alignments, can lead to variations in the appropriate δ_2 for data analysis of such samples. This problem can be minimized in an alternative calibration in which δ_2 is measured with the sample in place after the offset and phase angle calibration, but before the spectral response calibration.

5.1. Retardance calibration

In general, an internal alignment procedure is necessary to ensure that the fast axes of the two plates of each MgF_2 biplate compensator are precisely orthogonal, and thereby to minimize artifacts in their retardance spectra [16,17]. Here, it is assumed that such a procedure has been performed for both compensators. For measurements in the straight-through $PC_{1r}(5\omega)C_{2r}(3\omega)A$ configuration, in the absence of errors, only the Fourier coefficients in Eq. (2) with $n=2$, 4, 6, 8 and 10 are non-zero. Under these conditions, the amplitudes of the measured $n=4$, 6 and 10 Fourier coefficients can provide δ_1 and δ_2 directly, according to:

$$\delta_1 = 2\tan^{-1}\left\{|B_8'|/|B_{12}'|\right\}^{1/2}, \tag{5a}$$

$$\delta_2 = 2\tan^{-1}\left\{|B_8'|/|B_{20}'|\right\}^{1/2}, \tag{5b}$$

where $|B_{2n}'| = \left[(\alpha_{2n}')^2 + (\beta_{2n}')^2\right]^{1/2}$ [15]. Eqs. (5a) and (5b) do not employ phase-corrected coefficients; thus, (C_{S1}, C_{S2}) are not required for this calibration. Fig. 2a,b show the resulting spectra in δ_1 and δ_2 The solid line fits adopted for subsequent data reduction assume that the birefringence of MgF_2 is a fourth-order polynomial in photon energy. Quarterwave points of $E_{Q1}=3.594$ eV and $E_{Q2}=3.491$ eV are determined. The open and closed circles in Fig. 2c denote the differences between the experimental and best-fit spectra in δ_1 and δ_2, respectively. Maximum random deviations of $\sim\pm0.2°$ are observed; systematic deviations are smaller, $<\pm0.1°$.

5.2. Offset and phase angle calibration

The angular offsets and phase shifts can be determined in the actual $PC_{1r}(5\omega)SC_{2r}(3\omega)A$ configuration by combining data collected either in a separate step after sample mounting and alignment or during the actual sample measurement, i.e. in the self-calibration mode (most often using the starting sample surface prior to film growth or sample processing) [8,15]. In the offset

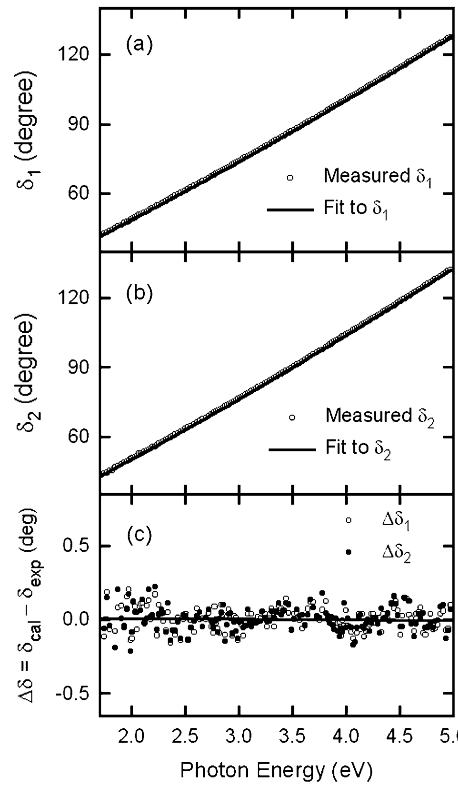

Fig. 2. Spectra in the compensator retardances (a) δ_1 and (b) δ_2, obtained experimentally in straight-through (points). The solid line fits in (a) and (b) are based a fourth-order polynomial in photon energy for the birefringence of MgF_2. The open and closed circles in (c) denote the differences between the experimental and best-fit spectra in δ_1 and δ_2.

and phase angle calibration, the following phase functions are exploited

$$\Theta'_{2n} = \tan^{-1}\left(\beta_{2n}'/\alpha_{2n}'\right) = \tan^{-1}\left(\beta_{2n}/\alpha_{2n}\right) + \phi_{2n};$$

$$n = 1, 2, \ldots, 8, 10, 11, 13, 16. \tag{6}$$

Quadrant corrections to the phase functions will be needed for self-consistent results. These corrections will depend on the instrument values (P', C_{S1}, C_{S2}, A'). It is useful to pre-align the fast axis of each compensator relative to its motor shaft to ensure that C_1' and C_2' are near zero at the onset of data collection $(t=0)$ for a reference pixel. In this way, approximate calibration values are known in advance. Although there are many possible ways of employing the phase functions for calibration, a procedure will be described here that works well for a nearly isotropic sample. Employing Θ_{2n}' with $n=2$, 4 and 8, the following expressions can be derived

$$P - P_S + 5C_{S1} = (1/4)(\Theta_4' + \Theta_{16}'), \tag{7a}$$

$$A - A_S + 3C_{S2} = (1/4)(\Theta_{16}' - \Theta_4'), \tag{7b}$$

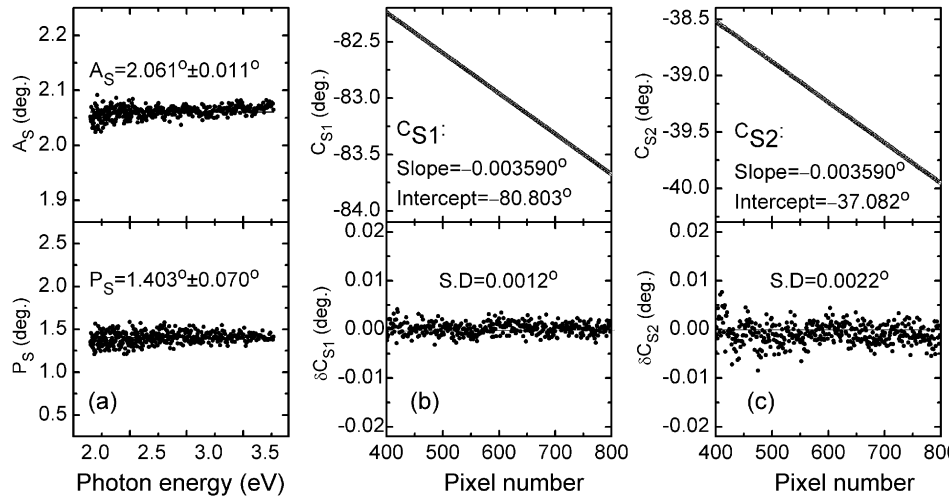

Fig. 3. (a) P_S and A_S vs. photon energy, including the spectral average and standard deviation (S.D.) range, and (b) C_{S1} and (c) C_{S2} vs. photodiode array pixel number, including the best linear fits and the differences between the experimental data and best fits. These results were measured in reflection from an isotropic a-Si:H film.

$$5C_{S1}-3C_{S2}=(1/2)(\Theta_8'-\Theta_4'). \tag{7c}$$

Eqs. (7a) and (7b) are valid for the most general Mueller matrix, whereas Eq. (7c) is valid only when $m_{23}=m_{32}$, e.g. for an isotropic sample in which case both of these elements vanish. A third equation is needed, and one of the following two functions is employed:

$$|B_6'|^2/|B_4'|^2 \approx \left\{\left[16\cos^4(\delta_1/2)\tan^2\Delta\right]/\sin^2\delta_1\right\} \times (P-P_S)^2; \quad P\approx P_S \tag{8a}$$

$$|B_{10}'|^2/|B_4'|^2 \approx \left\{\left[16\cos^4(\delta_2/2)\tan^2\Delta\right]/\sin^2\delta_2\right\} \times (A-A_S)^2; \quad A\approx A_S \tag{8b}$$

Eqs. (8a) and (8b) are valid for an isotropic sample with the polarizer and analyzer aligned near the p-direction, respectively. To employ these functions, the ellipsometric phase angle Δ for the sample must not be near 0° or $\pm$180°, and the amplitude ratio at the left of Eq. (8a) or Eq. (8b) is plotted as a function of the polarizer or analyzer reading near P_S or A_S, respectively. Such a plot is fitted to a parabola whose minimum occurs either at $P=P_S$ or at $A=A_S$. If P_S or A_S is determined in this way, then Eqs. (7a)–(7c) can be solved for the remaining three calibration angles.

As an example of calibration results applying Eqs. (7a)–(7c) and Eq. (8b), Fig. 3 shows (a) P_S and A_S vs. photon energy, and (b) C_{S1} and (c) C_{S2} vs. photodiode array pixel number as measured in reflection from isotropic amorphous silicon (a-Si:H). For these results, the array was operated without grouping. Because A_S in Fig. 3a is determined in a procedure in which the analyzer reading is stepped, it exhibits a lower standard deviation (approx. 0.01°) than that of P_S (approx. 0.07°). In Fig. 3b–c, C_{S1} and C_{S2} exhibit linear relationships vs. pixel number over the $k=400$–800 pixel range with identical slopes $-0.003590°$ to within $(1\times10^{-6})°$. These linear relationships arise because the time origins for the readout of successive pixels are offset by the single pixel readout time t_x of 5 μs. The slopes of the linear fits in Fig. 3b–c are in close agreement with the expected value of $\omega t_x=-0.0036°$. The difference can be ascribed to a stable motor speed of 1.994 Hz (rather than 2 Hz). Agreement in the measured slopes of C_{S1} and C_{S2} in successive calibrations over long periods attests to the high stability of the 5:3 frequency ratio [15].

5.3. Spectral response calibration

For a sample measured in transmission or reflection, in the absence of depolarizing effects, M_{11} is the specular transmittance or reflectance for incident unpolarized light. The critical step in the measurement of M_{11} is the determination of the ellipsometer spectral response function I_{00} [8,15]. In the transmission geometry, I_{00} can be obtained easily by removing the sample; in this case, $M_{11}=1$ so $I_{00}=I_0/a_0$. For a real time measurement in reflection, if the nature of the initial starting surface at $t=0$ is known, then this surface can be employed as a calibration standard for subsequent measurements. Using this approach, one can write:

$$M_{11}(t)=\frac{I_0'(t)a_0(0)}{I_0'(0)a_0(t)}R_u(0) \tag{9}$$

where $I_0'(0)$ and $I_0'(t)$ are the measured d.c. components of the waveform obtained from the known starting surface at $t=0$ and from the unknown surface at time t, respectively. The a_0 spectra are obtained for the corresponding surfaces after substituting the Fourier coefficients $(\alpha_{2n}', \beta_{2n}')$ into Eq. (3), and in turn substituting the transformed coefficients into Eq. (4a). Finally, $R_u(0)=M_{11}(0)$ and $M_{11}(t)$ are the assumed known and unknown (1,1) elements of the unnormalized Mueller matrices for the surface at $t=0$ and time t, respectively.

6. Mueller matrix conversion to complex amplitude ratios

Determination of the three complex amplitude ratios from the Mueller matrix starts from the Jones-to-Mueller conversion equation [18],

$$\mathbf{M}_P=\mathbf{A}\cdot(\mathbf{J}\otimes\mathbf{J}^*)\cdot\mathbf{A}^{-1}, \tag{10}$$

where $\mathbf{M}_P$ is the Mueller matrix assuming a perfect, i.e. non-depolarizing, sample. In the reflection geometry, $\mathbf{J}$ is the unnormalized Jones matrix with elements $J_{11}=r_{pp}$, $J_{12}=r_{ps}$, $J_{21}=r_{sp}$, and $J_{22}=r_{ss}$. Thus, the following definitions have been adopted for the reflection coefficients: $r_{jj}\equiv[(E_r)_j/(E_i)_j]_{(E_i)_i=0}$ and $r_{ij}\equiv[(E_r)_i/(E_i)_j]_{(E_i)_i=0}$, where the inner subscripts indicate the reflected (r) and incident (i) electric fields and the outer subscripts (i, j) denote the possible combinations of (p, s) or (s, p) directions. Finally, in Eq. (10), $\mathbf{A}$ is the 4×4 Jones-to-Mueller conversion matrix with $A_{11}=A_{14}=A_{21}=-A_{24}=A_{32}=A_{33}=1$, $A_{42}=-A_{43}=i$, and with all other elements $A_{ij}=0$ (adopting the $e^{i\omega t}$ time convention for the electric fields as in Ref. [18]). If one allows the possibility of sample imperfections that generate completely *random* depolarization, then

$$\mathbf{M}=p\mathbf{M}_P+(1-p)\mathbf{M}_D, \tag{11}$$

where $\mathbf{M}_D$ is the Mueller matrix for a perfect depolarizer [$(\mathbf{M}_D)_{11}=M_{11}$; all other elements $(\mathbf{M}_D)_{ij}=0$], and p describes the fraction of the polarized irradiance reflected from the sample [19].

Substitution of Eq. (10) along with the measured normalized elements of $\mathbf{M}$, $m_{ij}=M_{ij}/M_{11}$, into Eq. (11) followed by inversion yields expressions for the complex amplitude reflection ratios $\rho_{pp}\equiv r_{pp}/r_{ss}=\tan\psi_{pp}\exp(i\Delta_{pp})$, $\rho_{sp}\equiv r_{sp}/r_{ss}=\tan\psi_{sp}\exp(i\Delta_{sp})$, and $\rho_{ps}\equiv r_{ps}/r_{ss}=\tan\psi_{ps}\exp(i\Delta_{ps})$ that define $\mathbf{M}_P$:

$$\rho_{pp}=[(m_{33}+m_{44})+i(m_{34}-m_{43})]/D_1, \quad \text{(LR)} \tag{12a}$$

$$\rho_{sp}=[(m_{13}-m_{23})+i(m_{14}-m_{24})]/D_1, \quad \text{(UR)} \tag{12b}$$

$$\rho_{ps}=[(m_{31}-m_{32})-i(m_{41}-m_{42})]/D_1, \quad \text{(LL)} \tag{12c}$$

where

$$D_1=p-m_{12}-m_{21}+m_{22} \tag{12d}$$

At the right of Eqs. (12a)–(12c) 'LR', 'UR', and 'LL' indicate that the numerator is evaluated from the lower right, upper right, and lower left 2×2 blocks of $\mathbf{M}$.

The parameter p is also derived in the inversion, yielding an expression that utilizes all 15 elements of the normalized Mueller matrix:

$$p=(b^2+c)^{1/2}-b, \tag{13a}$$

$$b=(m_{22}-m_{12}-m_{21})/3, \tag{13b}$$

$$\begin{aligned}c=[&(m_{22}-m_{12}-m_{21})^2+(m_{13}-m_{23})^2+\\&(m_{14}-m_{24})^2+(m_{31}-m_{32})^2+(m_{41}-m_{42})^2+\\&(m_{34}-m_{43})^2+(m_{33}+m_{44})^2]/3.\end{aligned} \tag{13c}$$

This parameter can be used, for example, to account for the collection of multiply-scattered light by the polarization detection arm, an effect that may occur in the measurement of sculptured thin films due to sample imperfections such as macroscopic roughness or void structures (see Section 7). The parameter may also be used to simulate the effect of spectrograph stray light, an ellipsometer imperfection [20]. In fact, the second term at the right in Eq. (11) gives rise to an additional d.c. irradiance contribution at the detector, i.e. above that generated by a perfect sample, and the stray light contribution at the detector is expected to appear similarly in form.

Second independent expressions for the off-diagonal amplitude reflection ratios can be derived using more involved expressions from combinations of Mueller matrix blocks:

$$\begin{aligned}\rho_{sp}=\{&(m_{33}+m_{44})[(m_{31}+m_{32})+i(m_{41}+m_{42})]\\&-(m_{34}-m_{43})[(m_{41}+m_{42})\\&-i(m_{31}+m_{32})]\}/D_1D_2, \quad \text{(LL+LR)}\end{aligned} \tag{14a}$$

$$\begin{aligned}\rho_{ps}=\{&(m_{33}+m_{44})[(m_{13}+m_{23})-i(m_{14}+m_{24})]\\&+(m_{34}-m_{43})[(m_{14}+m_{24})\\&+i(m_{13}+m_{23})]\}/D_1D_2, \quad \text{(UR+LR)}\end{aligned} \tag{14b}$$

where

$$D_2=p+m_{12}+m_{21}+m_{22}. \tag{14c}$$

Only the amplitude squares of the complex reflection ratios can be deduced from the upper left block:

$$|\rho_{pp}|^2 = D_2/D_1, \quad \text{(UL)} \tag{15a}$$

$$|\rho_{sp}|^2 = (p + m_{12} - m_{21} - m_{22})/D_1, \quad \text{(UL)} \tag{15b}$$

$$|\rho_{ps}|^2 = (p - m_{12} + m_{21} - m_{22})/D_1, \quad \text{(UL)}. \tag{15c}$$

It is of interest to consider very weak anisotropy, for example, that induced at the surface of a cubic semiconductor [21]. Then in Eqs. (12a)–(12d) and Eqs. (15a)–(15c), $D_1 \approx 4\cos^2\psi_{pp}$, and so measurements of weak anisotropy will fail when $\psi_{pp} \approx 90°$. Similarly in Eqs. (14a)–(14c), $D_1 D_2 \approx 4\sin^2 2\psi_{pp}$ and these measurements will fail when $\psi_{pp} \approx 0°$ or 90°. Finally, Eqs. (15b) and (15c) are insensitive to the presence of weak anisotropy owing to the measurement of amplitude-squared ratios.

7. Applications

Three different sets of results from the dual rotating-compensator multichannel ellipsometer will be presented: (i) assessment of the isotropy of an a-Si:H film prepared by plasma-enhanced chemical vapor deposition (PECVD); (ii) measurement of the surface-induced optical anisotropy in (110) Si; and (iii) measurement of the local form birefringence of a chiral thin film.

Fig. 4 shows the normalized Mueller matrix elements from the 2×2 URB and LLB for a PECVD a-Si:H film measured in reflection at an angle of incidence of $\theta_i = 69.90 \pm 0.05°$. The calibration data obtained prior to this measurement are given in Fig. 3. For an isotropic sample such as this one, the 8 depicted matrix elements should vanish. The waveform spectra used for the determination of the entire Mueller matrix for a-Si:H were obtained as an average of 20 optical cycles, yielding an overall acquisition time of 5 s. Fig. 4 shows that the spectrally-averaged values of the eight depicted Mueller matrix elements are 1×10^{-3} or less, and the spectral standard deviations are 3×10^{-3} or less. Such results attest to the very high accuracy of the multichannel instrument, as will be discussed further in the second demanding application.

Fig. 5 shows all normalized Mueller matrix elements for a (110) Si wafer surface measured in reflection at $\theta_i = 69.90 \pm 0.05°$. These spectra were collected in 12 s, taking an average of 48 detector waveforms over 24 mechanical cycles. In this case, the sample was etched in situ in a windowless cell using 5 vol.% HF in methanol and was subsequently measured under N_2 gas flow in order to maintain a clean surface. The wafer was oriented for a ~45° angle, denoted ϕ, between the [001] principal axis in the sample surface and the line of intersection of the plane of incidence with the surface. For this surface the eight elements of the 2×2 URB

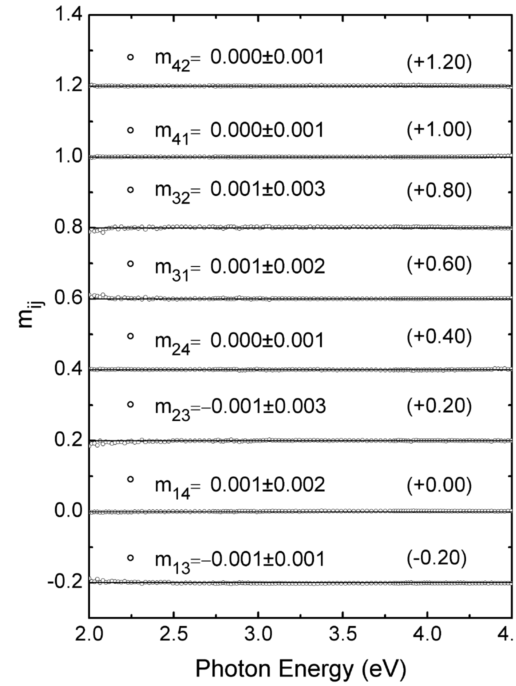

Fig. 4. Normalized Mueller matrix elements from the 2×2 URB and LLB for a-Si:H measured in reflection at an angle of incidence of $\theta_i = 69.90 \pm 0.05°$. The waveform spectra were obtained as an average of 20 optical cycles, for an overall acquisition time of 5 s.

and LLB of the Mueller matrix do not vanish, but show maximum amplitudes of $\sim 6 \times 10^{-3}$, attributed to surface-induced optical anisotropy. In support of this interpretation, the amplitudes of these matrix elements vanish when the sample is rotated so that the angle ϕ is ~0 or 90°.

Fig. 6 shows the results for ρ_{pp}, ρ_{ps}, ρ_{sp}, and p derived from the Mueller matrix under the same measurement conditions as Fig. 5, combining selected results from Eq. (12a)–Eq. (12d), Eq. (13a)–Eq. (13c), Eq. (14a)–Eq. (14c), and Eq. (15a)–Eq. (15c). In Fig. 6, ρ_{pp} was obtained from Eq. (12a), whereas the low energy (<3 eV) parts of Re(ρ_{sp}) and Re(ρ_{ps}) were obtained from Eqs. (14a) and (12c), respectively. For Re(ρ_{sp}) and Re(ρ_{ps}) at higher energy and for Im(ρ_{sp}) and Im(ρ_{ps}) over the full energy range, the results from Eqs. (12b) and (12c) were averaged with those of Eqs. (14a) and (14b), respectively. This overall approach provided the highest accuracy spectra in ρ_{sp} and ρ_{ps}. In fact, for a very thin uniaxial surface layer, it can be shown that $\rho_{sp} = -\rho_{ps}$ [22], and Fig. 6 reveals this characteristic at a high level of accuracy, within $\sim 1 \times 10^{-4}$. Finally, the deviations of p from unity in Fig. 6 are attributed to instrument imperfections, dominated in this case by spectrograph stray light. Allowing p to deviate from unity in the analysis has no effect on the determination of ρ_{ps} and ρ_{sp}; however, it significantly improves the agreement of the ψ_{pp} spectra obtained independently

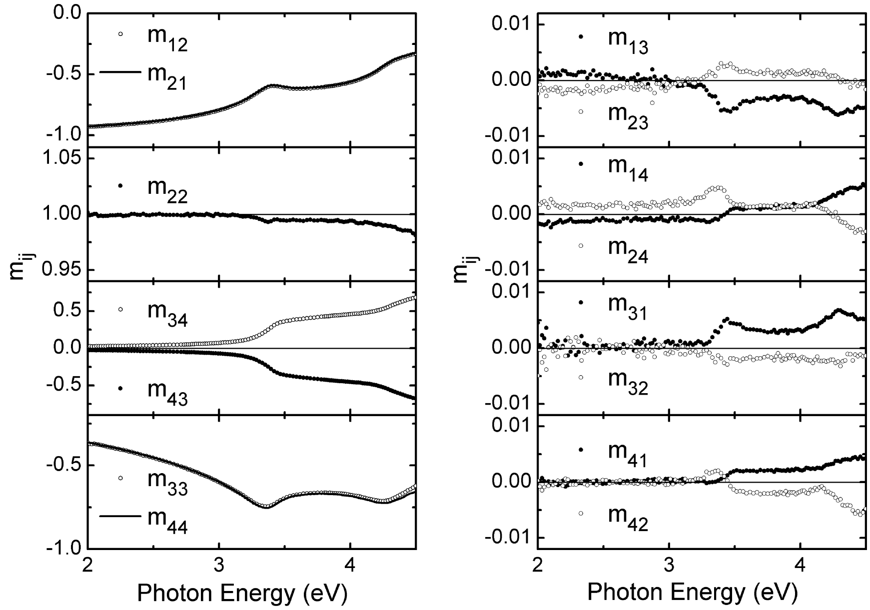

Fig. 5. Normalized Mueller matrix elements for a clean (110) Si wafer surface measured in reflection at $\theta_i = 69.90 \pm 0.05°$. The waveform spectra were obtained as an average of 48 optical cycles, for an overall acquisition time of 12 s.

from Eqs. (12a) and (15a), reducing the difference at 3.5 eV, for example, from 0.2 to 0.05°. Interpretation of the spectra in ρ_{pp}, ρ_{ps}, and ρ_{sp} of Fig. 6 in terms of the bulk isotropic and surface anisotropic optical properties will be provided in a separate article in these Proceedings [23].

Fig. 7 shows all normalized Mueller matrix elements measured in transmission at normal incidence for a 4.7 μm thick MgF_2 chiral thin film deposited by glancing angle deposition with simultaneous substrate rotation. A total of 12.3 turns yields a right-handed helicoidal structure (counterclockwise rotation in progression from substrate to film surface) with a pitch of 0.382 μm. The spectra in Fig. 7 were derived from an average of 10 detector waveforms for an acquisition time of 2.5 s. In the absence of optical anisotropy, the Mueller matrix should revert to the identity matrix. The dominant feature of anisotropy present in all off-diagonal Mueller matrix elements is a resonance analogous to the Cotton effect [24] near $\lambda_0 = 440$ nm or $E_0 = 2.8$ eV. This resonance occurs when the wavelength of light in the material λ/n_{av}, matches the helicoid pitch P. Here, n_{av} is the average of the two principal indices of refraction that describe the local uniaxial structure. At the resonance, the electric field vector for left-circularly polarized light rotates spatially in phase with the right-handed helicoids when the sample is illuminated from the ambient side, as is the case here. Applying the expression $n_{av} = \lambda_0/P$, yields $n_{av} = 1.16$ which is consistent with the large volume fraction of voids (0.58) estimated for this film [25].

Fig. 8 shows the results for the complex amplitude transmission ratios τ_{pp}, τ_{sp}, and τ_{ps}, derived from the Mueller matrix of Fig. 7 combining the expressions from Eqs. (12a)–(12d), Eqs. (13a)–(13c), Eqs. (14a)–(14c) and Eq. (15a) (but with ρ replaced by τ). In these plots, which focus on the spectra in the resonance

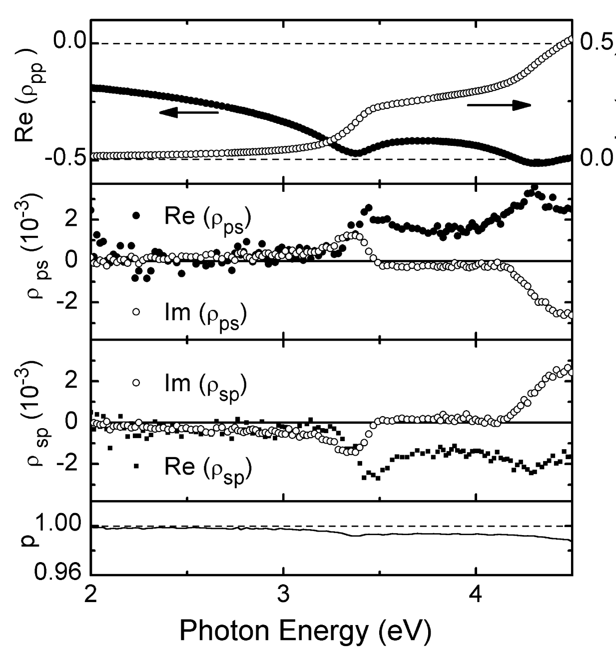

Fig. 6. Results for ρ_{pp}, ρ_{ps}, ρ_{sp}, and p derived from the Mueller matrix for clean (110) Si obtained from Eqs. (12a)–(12d), Eqs. (13a)–(13c) and Eq. (14a).

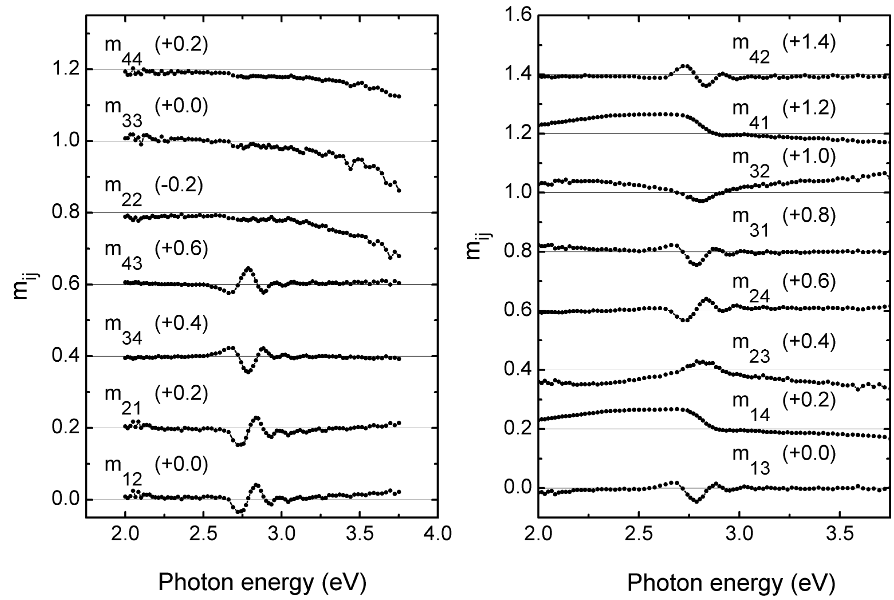

Fig. 7. Normalized Mueller matrix elements measured in transmission at normal incidence for a 4.7-μm thick MgF_2 chiral thin film. The waveform spectra were obtained as an average of 10 optical cycles, for an overall acquisition time of 2.5 s.

region, the real and imaginary parts of τ_{sp} and τ_{ps} have been obtained in two different ways, as has $|\tau_{pp}|^2 = \tan^2\psi_{pp}$. Results designated τ_{sp} and τ_{ps} have been obtained from the analogs of Eqs. (12b) and (12c), whereas those designated τ_{sp1} and τ_{ps1} have been obtained from the analogs of Eqs. (14a) and (14b). In addition, the results for $|\tau_{pp}|^2$ have been obtained either by computing the modulus of τ_{pp} as in Eq. (12a), or directly as in Eq. (15a). Overall excellent agreement is found for results calculated independently from different parts of the Mueller matrix. It is clear that higher quality results are obtained for $\mathrm{Re}(\tau_{sp})$ and $\mathrm{Re}(\tau_{ps})$ by applying

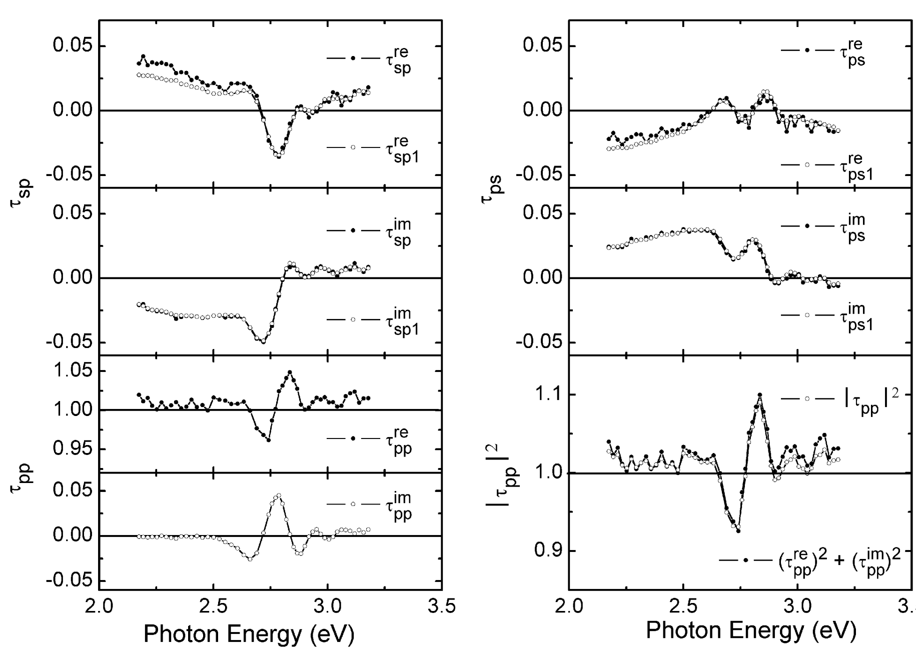

Fig. 8. Results for τ_{pp}, τ_{sp}, and τ_{ps}, derived from the Mueller matrix of Fig. 7 for the MgF_2 chiral thin film. Results designated τ_{sp} and τ_{ps} have been obtained from the analogs of Eqs. (12a)–(12d) whereas those designated τ_{sp1} and τ_{ps1} have been obtained from the analogs of Eqs. (14a)–(14c). The results for $|\tau_{pp}|^2$ have been obtained by computing the modulus of τ_{pp} as in Eq. (12a) (solid points), and directly as in Eq. (15a) (open points).

Eqs. (14a)–(14c); however, equally good data can be obtained for Im(τ_{sp}) and Im(τ_{ps}) either from Eqs. (12a)–(12d) or from Eqs. (14a)–(14c). In fact, the agreement of these latter two pairs of spectra [within $\sim(1-3)\times10^{-4}$] is remarkable considering their relatively low amplitude and different origin. The analysis of the spectra of Fig. 8 in terms of the structure and optical properties of the chiral film is beyond the scope of the present article and will be treated elsewhere [26]. To summarize, such modeling has shown that a birefringence $\Delta n(\lambda_0)$ of 0.066 associated with the local uniaxial structure is required to generate the observed magnitudes of the features in τ_{pp}, τ_{sp}, and τ_{ps} in Fig. 8.

8. Conclusions

A multichannel ellipsometer in the dual rotating-compensator configuration has been designed and constructed using optical elements fabricated from MgF_2 to ensure a wide spectral range, e.g. making it possible to add a D_2 lamp to the standard Xe lamp in the next generation design. For a dual rotating-compensator system in which the two compensators are rotated at (ω_1, ω_2), the ($2\omega_1$, $4\omega_1$) and ($2\omega_2$, $4\omega_2$) as well as the eight sum and difference frequencies are present in the detected waveform for the most general Mueller matrix of a transmitting or reflecting sample. At the 5:3 ratio for ω_1:ω_2 used here, these include the $2n\omega$ frequencies where $n=1, 2, 3\ldots, 8, 10, 11, 13$ and 16, and where $\omega/2\pi=2$ Hz. Spectra in all 16 Mueller matrix elements of a transmitting or reflecting sample can be determined from the resulting 25 non-zero Fourier coefficients acquired in $(\pi/\omega)=250$ ms. In the data reduction to extract the Mueller matrix, calibration results are employed including the polarizer and analyzer offset angles (P_S, A_S) and the two spectra each in the compensator phase angle (C_{S1}, C_{S2}) and retardance (δ_1, δ_2).

In high speed Mueller matrix analysis, this research has focused on weakly anisotropic samples, including the (110) Si surface measured in reflection and nanostructured thin films measured in transmission, as demanding initial test cases. In these studies, the equation relating the Mueller and Jones matrices, including possible random depolarization to correct for instrument imperfections, is inverted so that (ρ_{pp}, ρ_{ps}, ρ_{sp}) [or (τ_{pp}, τ_{ps}, τ_{sp})] that define the (2,2)-normalized complex Jones matrix can be obtained from the Mueller matrix by multiple methods. For example, in the case of (110) Si where $\rho_{ps}=-\rho_{sp}$, the surface-induced anisotropic dielectric response $\Delta\varepsilon$ can be extracted by four different methods. Averaging the results obtained by these methods provides accuracy at the level of 10^{-4} in ρ for simultaneous real time determination of bulk isotropic and surface anisotropic optical responses of crystalline semiconductors.

Acknowledgments

The authors acknowledge support of NSF (Grant Nos. DMR-9820170 and DMR-0137240) and NREL (Subcontract Nos. XAF-8-17619-22 and AAD-9-18-668-09).

References

[1] R.W. Collins, D.E. Aspnes, E.A. Irene (Eds.), Proceedings of the 2nd International Conference on Spectroscopic Ellipsometry, (Elsevier, Amsterdam, 1998), also published as Thin Solid Films 313–314 (1998); see also these Proceedings.
[2] R.W. Collins, Rev. Sci. Instrum. 61 (1990) 2029.
[3] P.S. Hauge, Surf. Sci. 96 (1980) 108.
[4] J. Lee, P.I. Rovira, I. An, R.W. Collins, Rev. Sci. Instrum. 69 (1998) 1800.
[5] R.M.A. Azzam, Opt. Lett. 2 (1978) 148.
[6] P.S. Hauge, J. Opt. Soc. Am. 68 (1978) 1519.
[7] D.H. Goldstein, Appl. Opt. 31 (1992) 6676.
[8] R.W. Collins, J. Koh, J. Opt. Soc. Am. A 16 (1999) 1997.
[9] R.C. Thompson, J.R. Bottinger, E.S. Fry, Appl. Opt. 19 (1980) 1323.
[10] A.J. Hunt, D.R. Huffman, Rev. Sci. Instrum. 44 (1973) 1753.
[11] B.W. Bell, Opt. Eng. 28 (1989) 114.
[12] R. Anderson, Appl. Opt. 31 (1992) 11.
[13] W.M. McClain, W.H. Jeng, B. Pati, Y. Shi, D. Tian, Appl. Opt. 33 (1994) 1230.
[14] G.E. Jellison Jr, F.A. Modine, Appl. Opt. 36 (1997) 8184.
[15] J. Lee, J. Koh, R.W. Collins, Rev. Sci. Instrum. 72 (2001) 1742.
[16] D.E. Aspnes, Appl. Opt. 10 (1971) 2545.
[17] J. Lee, P.I. Rovira, I. An, R.W. Collins, J. Opt. Soc. Am. A 18 (2001) 1980.
[18] R.M.A. Azzam, N.M. Bashara, Ellipsometry and Polarized Light, North-Holland, Amsterdam, 1977.
[19] G.E. Jellison Jr, F.A. Modine, Appl. Opt. 36 (1997) 8190.
[20] I. An, R.W. Collins, Rev. Sci. Instrum. 62 (1991) 1904.
[21] D.E. Aspnes, J. Vac. Sci. Technol. B 3 (1985) 1498.
[22] K. Hingerl, D.E. Aspnes, I. Kamiya, L.T. Florez, Appl. Phys. Lett. 63 (1993) 885.
[23] C. Chen, I. An, R.W. Collins, These Proceedings.
[24] M.A. Cotton, C.R. Hebdo. Acad. Sci. (Paris) 120 (1895) 989.
[25] P.I. Rovira, R.A. Yarussi, R.W. Collins, V.C. Venugopal, A. Lakhtakia, R. Messier, K. Robbie, M.J. Brett, Thin Solid Films 313–314 (1998) 373.
[26] N.J. Podraza, C. Chen, I. An, G.M. Ferreira, P.I. Rovira, R. Messier, R.W. Collins, These Proceedings.